$Sb_2(S,Se)_3$-Based Thin Film Solar Cells: Numerical Investigation

A. Khadir[a,b,*]

[a] *Materials Science and Informatics Laboratory, University of Djelfa, Cité 05 Juillet route Moudjbara BP: 3117, 17000, Djelfa, Algeria*
[b] *Laboratory of Metallic and Semiconducting Materials, University of Biskra, BP 145 RP, 07000, Biskra, Algeria*

Received: 08.03.2023 & Accepted: 11.04.2023

Doi: 10.12693/APhysPolA.144.52 *e-mail: a.khadir@univ-djelfa.dz

Recently, antimony selenosulfide $Sb_2(S,Se)_3$-based thin film devices have received particular attention from the research community. Nevertheless, their experimental power conversion efficiency is still below 10.5%. In the present work, a numerical study of ZnO:Al/i-ZnO/CdS/$Sb_2(S,Se)_3$/spiro-OMeTAD/contact structure is carried out using a one-dimensional solar cell capacitance simulator. In this study, we focus on investigating the effect of the carriers' densities in main layers, selenium (Se) content in the absorber with different profiles, and using Cu_2O as an alternative hole transport layer. It is found that 10^{21}, 10^{15}, and 10^{21} cm^{-3} doping densities in CdS/absorber/hole transport layers, respectively, and gradient Se/(Se+S) content in the range of 0.8–0.9, with the use of Cu_2O as a hole transport layer, give a remarkable power conversion efficiency of 19.84%.

topics: $Sb_2(S,Se)_3$, gradient bandgap, Cu_2O, solar cell capacitance simulator (SCAPS)

1. Introduction

Chalcogenide compounds have gained particular success in the field of solar cells during the last decades owing to their high light-harvesting efficiency. Devices based on CdTe and $Cu_2(In,Ga)Se_2$ (CIGS) have attained champion power conversion efficiencies (PCE) higher than 22% with remarkable operational stability [1].

Although significant progress has been achieved using CdTe and CIGS, the cadmium toxicity with the indium and gallium scarcity disturbs the further development of thin-film devices based on these materials. In order to overcome the mentioned problems, researchers have begun explorations of new alternative compound materials, such as $Cu_2ZnSn(Se,S)_4$, Cu_2ZnSnS_4, $CuSbSe_2$ [2–4], $Sb_2(S,Se)_3$ [5–10], Sb_2Se_3 [11–14], and Sb_2S_3 [15–18], for the photovoltaic devices. These materials are favored due to their eco-friendliness and earth abundance. From the previous alternative materials, Sb_2Se_3 and Sb_2S_3 materials are usually obtained at temperatures below 400°C with fewer secondary phases [19].

The bandgaps of Sb_2Se_3 and Sb_2S_3, which have the same band structure, are 1.1 and 1.7 eV, respectively. Sb_2Se_3 and Sb_2S_3 can be mixed for any chosen x = Se/(Se+S) proportion to form a single-phase $Sb_2(Se_xS_{1-x})_3$ alloy with a tunable bandgap in the 1.1–1.7 eV range [10]. So, $Sb_2(Se_xS_{1-x})_3$ compound could reduce the fabrication cost of thin film solar cells. Hence, antimony selenosulfide ($Sb_2(S,Se)_3$) has been proposed as an ideal candidate for substitute light-absorption material due to its high light-absorption, possible band gap tuning, high absorption coefficient ($> 10^5$ cm^{-1}), earth abundance, non-toxicity, air stability and moisture [17, 20, 21].

To this day, antimony selenosulfide-based solar cells have recorded a 10.5% of conversion efficiency [22]. Various techniques for manufacturing antimony selenosulfide (Sb_2Se_3 and Sb_2S_3) solar cells have been reported, such as chemical bath deposition [23–24], sol–gel method [25, 26], hydrothermal approach [10, 27–30], thermal evaporation [31–34], spin-coating (Wu et al. [35]), vapor transport deposition (VTD) [36–41], closed-space sublimation (CSS) [42–44], magnetron sputtering [45–48], and a multi-source sequential co-evaporation [49]. From these techniques, the hydrothermal method is one of the most convenient in antimony selenosulfide-based devices processing, permitting to attain efficiencies above 10% for superstrate configuration [10, 22].

Many experimental works have been used to ameliorate the $Sb_2(Se_xS_{1-x})_3$-based devices' conversion efficiency. Conversion efficiencies of 5.47, 5.79, 5.8, 6.3, and 8.29% were reported by [31, 32, 35, 50, 51] with different Se fractions. R. Tang et al. [10], using the hydrothermal method in $Sb_2(S_{0.71},Se_{0.29})_3$

thin film deposition, achieved an encouraging efficiency of 10.0%. $Sb_2(S,Se)_3$-based devices with the highest PCE are realized by Wang et al. [22] using an in situ hydrothermal synthesis technique. Y. Pan et al. [37] have found that the area of vapor enlargement allows obtaining high-quality antimony selenosulfide films with large grains of preferred orientation. They processed $Sb_2(S,Se)_3$-based solar cells with 7.6% by appropriate tuning of the evaporation source area. X. Wang [9] reported that the use of potassium fluoride aqueous solution to chemically etch the antimony selenosulfide films decreases the interfacial defects on the one hand, and improves uniformity and crystalline structure on the other, which reduces the loss of carriers caused by recombination. Their chemically etched antimony selenosulfide-based solar cell showed an improvement in the current density and fill factor (FF), with a maximum conversion efficiency of 9.58% [9].

In parallel with experimental research, there has been a fast trend to study numerically the antimony selenosulfide-based devices. In line with this trend, numerous works were carried out in order to investigate the performance of antimony selenosulfide-based devices. T. Jeminez et al. [52] demonstrated a $Sb_2(S,Se)_3$-based solar cell conversion efficiency of 29% with Se gradient composition from 0.34 to 0.48 with thicknesses above 1.5 μm of $Sb_2(Se_xS_{1-x})_3$ absorber. M.M. Nicolãs-Marín [53] analyzed numerically a $Cd_{1-x}Zn_xS/Sb_2(Se_xS_{1-x})_3$-based solar cell structure, which demonstrated a 14.8% conversion efficiency, and then, due to a reduction of the buffer/absorber interface defects and series and shunt resistances, a 17.4% conversion efficiency. I. Gharibshahian et al. [54] studied the effect of the sulfur amount in both absorber and buffer layers on the performance of a based $Sb_2(Se_xS_{1-x})_3$/Zn(O,S) device. They found that by adjusting the sulfur composition in buffer and absorber layers, an $Sb_2(S_{0.2}Se_{0.8})_3/ZnO_{0.4}S_{0.6}$ structure showed a conversion efficiency of 15.65% [54]. M. Saadat et al. [55] investigated the charge carriers transport in the absorber/HTL interface of $Sb_2(S,Se)_3$-based solar cells in their theoretical simulation. They reported a 20.8% conversion efficiency at a Se/(Se+S) fraction of 0.6 and valence band maximum $VBM_{HTL} = 5.7$ eV, corresponding to $\Delta E_V \approx +0.39$ [55].

Improvement of the conversion efficiency can be achieved by investigating the doping concentration in the main layers [56] and increasing the absorption by using a bandgap grading of the absorber material [57]. The electron transport layer (ETL) and hole transport layers are also determinants in improving the solar cell performance by reducing recombination losses and then facilitating the carriers transport to the desired regions. Thus, the choice of the appropriate ETL materials is quite important [53, 54, 58]. As well, the selection of the probable HTL materials, namely molybdenum trioxide (MoO_3), copper(I) thiocyanate (CuSCN), copper(I) iodide (CuI), nickel oxide (NiO), and cuprous oxide (Cu_2O) is a crucial factor in improving the solar cell performance [6, 7, 59, 60, 61, 62].

In this work, we begin our research by optimizing the doping dose in the main layers of the proposed structure, followed by a study of the absorber uniform and graded bandgap effect on electrical parameters. Then, considering the availability and appropriateness, Cu_2O is being suggested and studied as a probable HTL for antimony selenosulfide-based devices.

2. Theory and models

Solar cells experimental processing costs time and material, thus, the numerical simulation based on physics has become extensively used because of its cheapness and quickness compared to experiment processing [63–65]. Information measure hardships encountered using experiments could be easily overcome using simulation. Herein, the numerical simulation processing is carried out using the one-dimensional (1D) solar cell capacitance simulator (SCAPS) [66]. In our study, we begin by simulating numerically the 10% efficiency structure fabricated by [10], then we make a comparison between the results. The aim of the comparison is the validation of our model. The structure of the simulated ZnO:Al/i-ZnO/CdS/$Sb_2(S_{1-x}Se_x)_3$/spiro-OMeTAD/contact is illustrated in Fig. 1. Materials' parameters used in the numerical simulation were chosen and selected carefully from numerous precedent works, and are listed in Table I [52–55]. For ZnO and CdS materials, we use the absorption coefficients from [66], while the absorption coefficients of $Sb_2(S_{1-x}Se_x)_3$ and spiro-OMeTAD were taken from [52] and [67], respectively. The defects of $Sb_2(S_{1-x}Se_x)_3$ were taken from [10]. At the (ETL, HTL)/absorber interfaces, we took a defect density

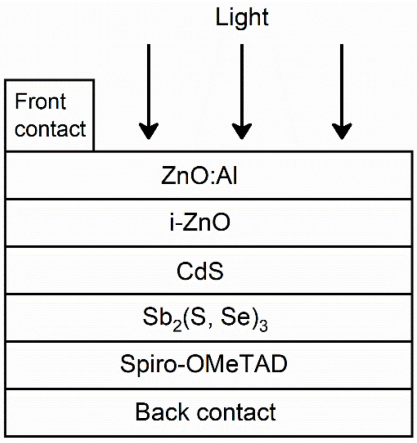

Fig. 1. Structure of the simulated $Sb_2(S,Se)_3$-based solar cell.

TABLE I

Parameters of materials used in simulation.

Parameter	ZnO:Al	i-ZnO	CdS	$Sb_2(S,Se)_3$	Spiro-OMeTAD
thickness [nm]	80	50	60	500	90
E_g [eV]	3.3	3.3	2.4	variable	2.88
χ [eV]	4.4	4.4	4.2	variable	2.05
ε	9	9	10	variable	3
N_C [cm^{-3}]	2.2×10^{18}	2.2×10^{18}	2.2×10^{18}	2.2×10^{18}	2.2×10^{18}
N_V [cm^{-3}]	1.8×10^{19}	1.8×10^{19}	1.8×10^{19}	1.8×10^{19}	1.8×10^{19}
v_{th}(n, p) [cm/s]	10^7	10^7	10^7	10^7	10^7
μ_n [cm^2/V s]	100	100	100	variable	2×10^{-4}
μ_p [cm^2/V s]	25	25	25	variable	2×10^{-4}
doping [cm^{-3}]	10^{19}	–	3×10^{17}	10^{14}	4×10^{18}

TABLE II

Properties of $Sb_2(S,Se)_3$ bulk and (ETL, HTL)/$Sb_2(S,Se)_3$ interfaces defects used in simulation.

Bulk defects of $Sb_2(S,Se)_3$			Defect of interfaces	
	Density [cm^{-3}]	Energy distr. [eV]		Density [cm^{-3}]
defect 1	1.3×10^{14}	0.5	ETL/$Sb_2(S,Se)_3$	1.4×10^{12}
defect 2	10^{15}	0.77	$Sb_2(S,Se)_3$/HTL	1.4×10^{12}

of 1.4×10^{12} cm^2, as presented in Table II [53]. The SCAPS simulator, which has options like batch calculations and up to 7 layers, is based on the drift-diffusion model for its operation, where it solves the Poisson equation alongside the continuity equation of electrons and that of holes. These can be written as follows

$$\frac{\partial^2 \Psi}{\partial x^2} = -\frac{q}{\varepsilon}\Big[p(x) - n(x) + N_{\mathrm{D}} - N_{\mathrm{A}} + p_t - n_t\Big], \tag{1}$$

$$\frac{1}{q}\frac{\mathrm{d}J_n}{\mathrm{d}x} = -G_{op}(x) + R(x), \tag{2}$$

$$\frac{1}{q}\frac{\mathrm{d}J_p}{\mathrm{d}x} = G_{op}(x) - R(x), \tag{3}$$

where ψ, ε_0, and ε_r denote the electrostatic potential, vacuum, and relative permitivities, respectively; p and n are the hole and electron concentrations. The donor and acceptor impurities are denoted with N_{D} and N_{A}, respectively. The generation and recombination rates are denoted by G and R, respectively. The device is irradiated with AM1.5 spectrum with the incident power density of 100 mW/cm^2 at room temperature.

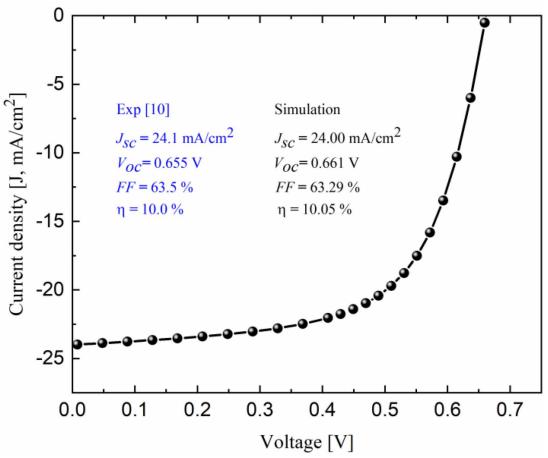

Fig. 2. J–V characteristics of the proposed antimony selenosulfide-based solar cell.

3. Results and discussions

As a first step, a comparison study between our proposed structure and that of experimental work is effectuated. By fine-tuning the most important parameters, the J–V characteristics reported by [10] are reproduced numerically, as shown in Fig. 2. This figure shows a good agreement between our results and those reported experimentally, which validates our model. Figure 3 depicts the resulting energy band diagram belonging to the studied ZnO:Al/i-ZnO/CdS/$Sb_2(S_{1-x}Se_x)_3$/spiro-OMeTAD/contact structure under the equilibrium condition. From this figure, we notice that the conduction band of CdS is lower than that of antimony selenosulfide. It is clearly seen that in the interface between CdS and antimony selenosulfide, the conduction band offset (CBO) is cliff-like, and it is equal to 0.4 eV, which favors the carriers' loss. On the other hand, the valence band offset (VBO) at the CdS/$Sb_2(S,Se)_3$ interface is equal to 1.365 eV.

The doping concentration in the main layers of thin film devices is of great importance and considerably affects their performance. Herein, we focus

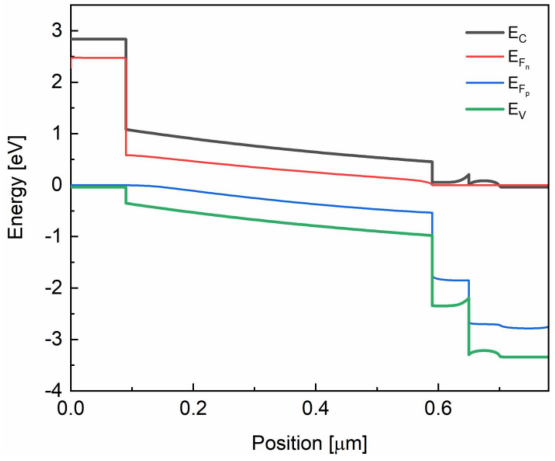

Fig. 3. Energy band diagrams of the proposed antimony selenosulfide-based device.

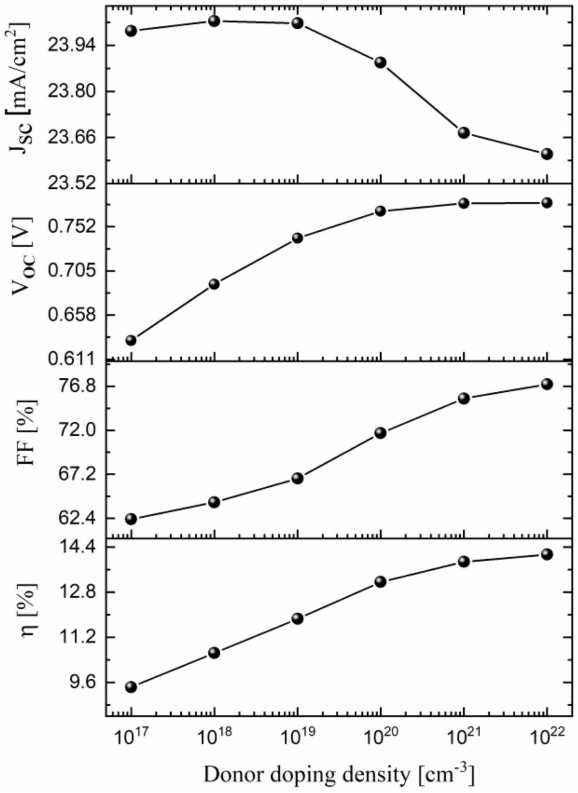

Fig. 4. Electrical parameters versus donor concentration in CdS layer.

on optimizing the doping dose in ETL (CdS), HTL (spiro-OMeTAD), and absorber ($Sb_2(S,Se)_3$) layers, respectively. Concerning the ETL layer, we vary the donor doping concentration from 10^{17} to 10^{22} cm^{-3} to see its effect on the device performance. Figure 4 illustrates the electrical parameters as a function of donor doping concentration. The doping dose augmentation affects first, in a positive sense, the short-circuit density up to 10^{18} cm^{-3}, and after this point, it tends to drop. The other electrical parameters are

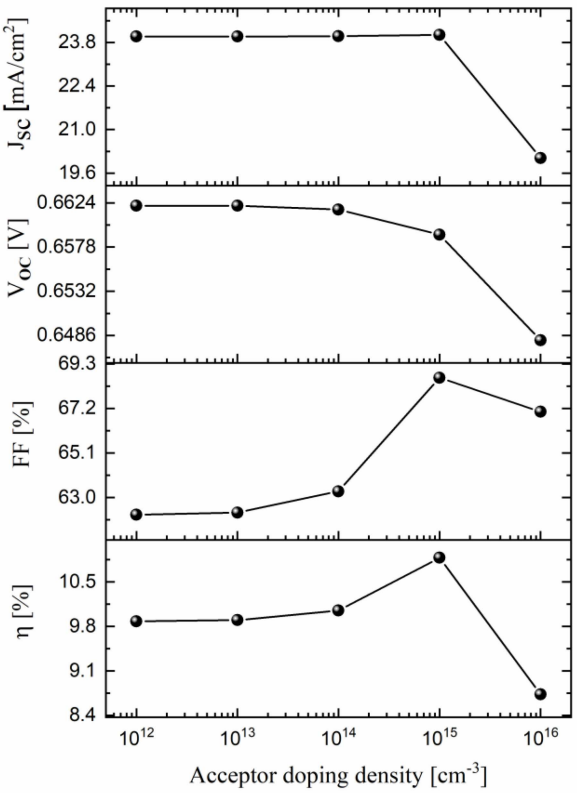

Fig. 5. Electrical parameters versus N_A in antimony selenosulfide layer.

affected positively; an increase in open-circuit voltage (V_{OC}), FF, and conversion efficiency (η) is detected. The enhancement of V_{OC} lasts till 10^{21} cm^{-3} doping concentration, where V_{OC} tends to become constant. At this point, the conversion efficiency attains 13.88%, so we take 10^{21} cm^{-3} as an optimized doping concentration value for the ETL layer. The enhancement of conversion efficiency is the result of the reverse saturation current density degradation caused by the N_D concentration augmentation in the ETL layer, as shown by

$$J_s = q\left(\frac{D_n}{L_n N_A} + \frac{D_p}{L_p N_D}\right) n_i^2. \quad (4)$$

A similar behavior is reported in [11, 68].

The absorbent layer, where most of the photons are supposed to be absorbed, is the key region in a thin film solar cell, and the acceptor doping density within it is a critical parameter that affects its performance. Hence, optimizing the acceptor density in this region is quite important. For this reason, a careful variation of N_A from 10^{12} to 10^{16} cm^{-3} in an antimony selenosulfide absorber is applied. The aim of this study is to show how the electrical parameters of the studied solar cell respond to this change in acceptor density. Figure 5 exhibits the curve of the targeted electrical parameters versus N_A. It is clearly seen from this figure that the short-circuit current density (J_{SC}) remains constant with N_A augmentation up

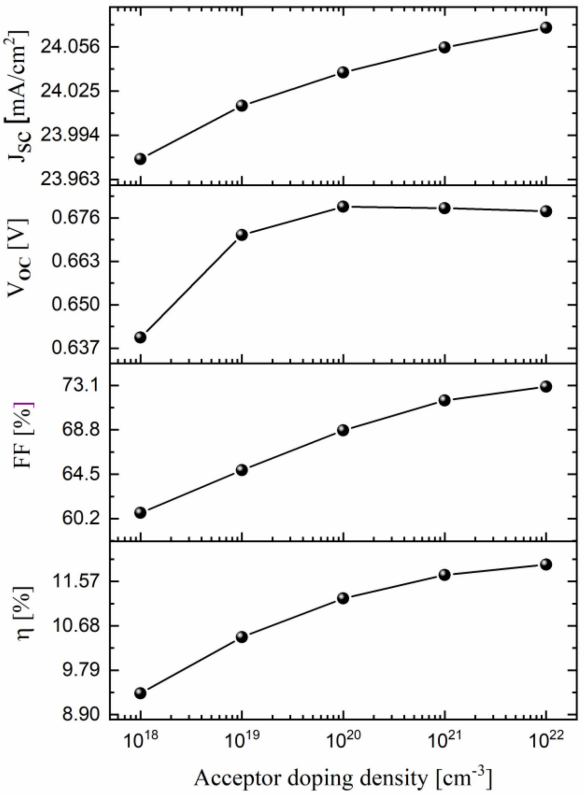

Fig. 6. Electrical parameters versus N_A in HTL (spiro-OMeTAD) layer.

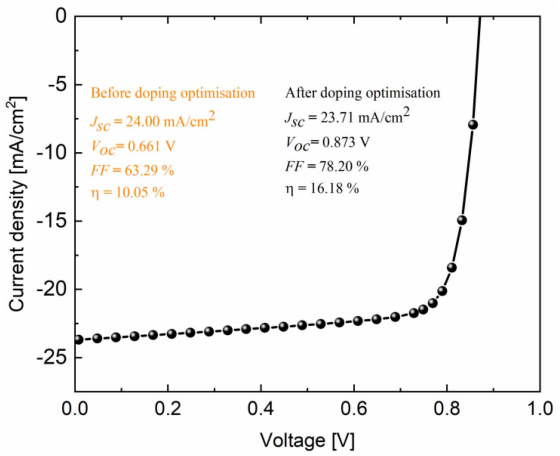

Fig. 7. J–V characteristics of the antimony selenosulfide-based devices after doping optimization.

to $N_A = 10^{15}$ cm^{-3}, after which it falls. For its part, the open-circuit voltage shows almost no change up to $N_A = 10^{14}$ cm^{-3}, and after this value, it begins to decrease slightly. Concerning the fill factor, we note that it increases with the acceptor doping augmentation up to $N_A = 10^{15}$ cm^{-3}, and after that, it starts to drop. The conversion efficiency also is enhanced with the increase in N_A, attaining a maximum value of 10.88% for N_A =10^{15} cm^{-3}. Similar behavior was reported in [11, 69, 70]. From the previous investigation, we reckon that an acceptor doping density in the range of 10^{14} to 10^{15} cm^{-3} is acceptable.

The surface recombination phenomenon in thin film solar cells has been considered as a real issue, leading to the use of HTL layers. As a consequence, HTL layers have shown their advantages in increasing the performance of solar cells. To enhance the role of the HTL layer, optimization of its acceptor doping density is also necessary. Therefore, we apply various doping densities ranging from 10^{18} to 10^{22} cm^{-3} in this region and record their effect on electrical parameters, as represented in Fig. 6. We notice from the curves in Fig. 6 that all of the electrical parameters enhance with the acceptor doping augmentation except for V_{OC}, where the increase lasts till $N_A = 10^{20}$ cm^{-3} to became constant till $N_A = 10^{21}$ cm^{-3}, after which a slight decrease is noticed. So, an acceptor doping density in the range of 10^{20} to 10^{21} cm^{-3} is desirable. These results are in accordance with those reported in [71]. We choose $N_A = 10^{21}$ cm^{-3} as an appropriate acceptor doping density in the HTL layer, which gives a conversion efficiency value of 11.70%. This enhancement in the solar cell performance is explained by the fact that the high doping of the HTL layer decreases the back contact resistance, increases the built-in voltage, inhibits carrier recombination, and thus enhances the charge collection.

Figure 7 shows the J–V characteristics using the chosen doping densities after optimization; $N_D = 10^{21}$ cm^{-3}, $N_A = 10^{15}$ cm^{-3}, and $N_A = 10^{21}$ cm^{-3} in ETL, absorber, and HTL layers, respectively. The curve in the figure shows the remarkable performance enhancement of the antimony selenosulfide-based device. The values 23.71 mA/cm^2, 0.873 V, 78.20%, and 16.18% are obtained for J_{SC}, V_{OC}, FF, and η, respectively.

Different uniform Se contents from 0 ($x = 0$) to 100% ($x = 1$) in $Sb_2(S_{1-x}Se_x)_3$ were simulated by taking into consideration the optimized doping densities found previously. The effect of selenium content on the electrical parameters is presented in Fig. 8. We note a continuing increase in J_{SC} with Se content augmentation, which is caused by the bandgap reduction of antimony selenosulfide, which allows for more photons of longer wavelengths to be absorbed. As depicted in this figure, V_{OC} drops with the selenium content augmentation, which is logical since the open-circuit voltage is a function of the bandgap [72]. The fill factor is affected positively by the selenium content augmentation, as shown in Fig. 8. The conversion efficiency simultaneously enhances with Se content augmentation, where it attains a maximum value of 17.55% for a selenium fraction of $x = 0.7$. Our results are in accordance with those reported in [8, 52, 54, 55].

The use of materials with graded bandgap as absorbers in thin film solar cells has shown a significant impact in enhancing their absorbance and

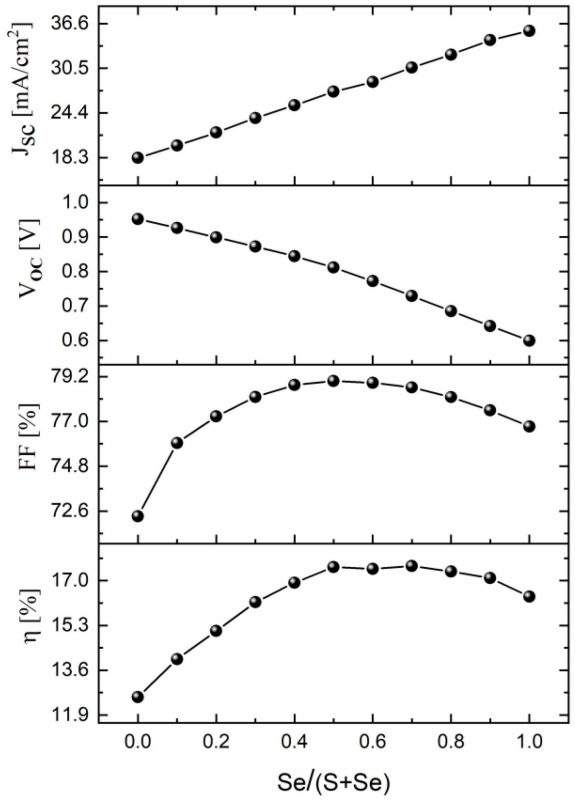

Fig. 8. Electrical parameters as a function of uniform Se/(S+Se) fraction in $Sb_2(S_{1-x}Se_x)_3$.

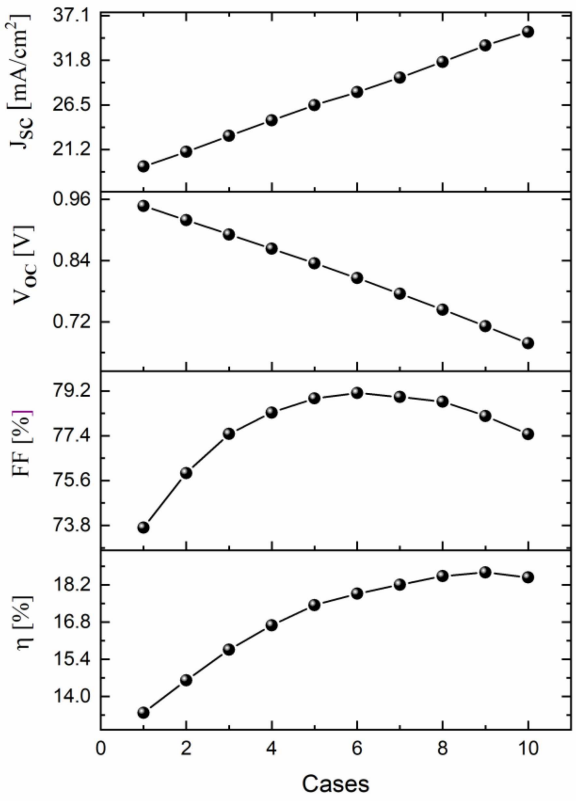

Fig. 9. Electrical parameters as a function of Se gradient cases in antimony selenosulfide layer.

hence their performance [57]. In this regard, we apply a double-graded bandgap in the absorber region of antimony selenosulfide-based devices using the optimized doping densities. We consider here gradient selenium contents ranging from 0–0.1, 0.1–0.2, to 0.9–1, i.e., 10 cases. It is noted that the absorber with a higher band gap is being put forward, while the one with a lower band gap is put downward in the solar cell under load. The effect of the double-graded bandgap on the electrical parameters of the $Sb_2(S,Se)_3$-based solar cell for the ten cases is illustrated in Fig. 9. The figure shows that the double-graded bandgap of $Sb_2(S,Se)_3$ causes the enhancement of J_{SC}, FF, and η, while V_{OC} is affected negatively. The conversion efficiency attains a maximum value of 18.67% for a gradient selenium content in the range of 0.8–0.9. The obtained result reveals that the graded band gap in the absorber region enhances the absorption compared to absorbers with a uniform band gap. Consequently, the performance of devices with materials with graded bandgap as absorbers is enhanced, which is in accordance with [52, 73].

As discussed previously, the incorporation of HTL layers between the absorber and the rear contact affects deeply in a positive manner the performance of thin film solar cells. In this regard, in this part of our work, we propose the Cu_2O material as a probable candidate to replace spiro-OMeTAD in antimony selenosulfide-based devices. The antimony selenosulfide-based device with the optimized doping densities, double gradient bandgap, and Cu_2O as an HTL layer is studied numerically, and the resulting J–V characteristics are presented in Fig. 10. The electrical parameters extracted from the J–V characteristics in Fig. 10 clearly seem to be enhanced by the use of Cu_2O as a hole transport layer, except for FF which shows an apparent decrease. The conversion efficiency of the final optimized antimony selenosulfide-based device attains an encouraging value of 19.84%.

The energy band diagrams of the proposed and final optimized $Sb_2(S,Se)_3$-based solar cells are presented in Fig. 11. The differences in the diagrams clearly explain the enhancement of the final optimized solar cell. In the absorber region, the inclination of the antimony selenosulfide energy band has been increased due to the gradient selenium content within it, which enhances the built-in electric field. As a consequence, the photogenerated carriers' separation and collection are enhanced, and the carrier's recombination rate in antimony selenosulfide and then the loss are decreased; the same behavior is reported in [71]. We note that at the interface between CdS and antimony selenosulfide, the cliff-like CBO is reduced from 0.4 eV in the proposed cell to 0.228 eV in the final optimized cell, leading to a lowering loss of carriers at the interface.

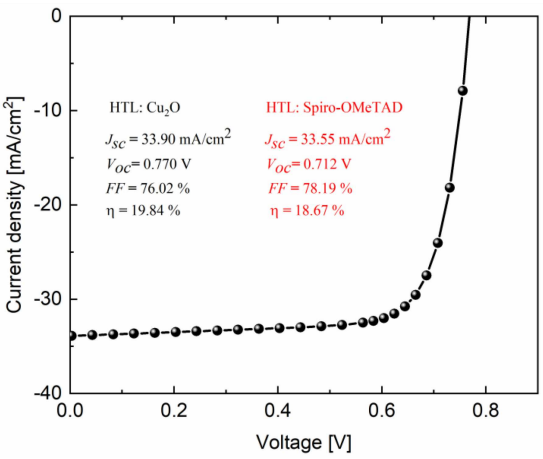

Fig. 10. J–V characteristics of the $Sb_2(S,Se)_3$-based solar cell after doping and gradient selenium content optimization with the use of Cu_2O as HTL layer.

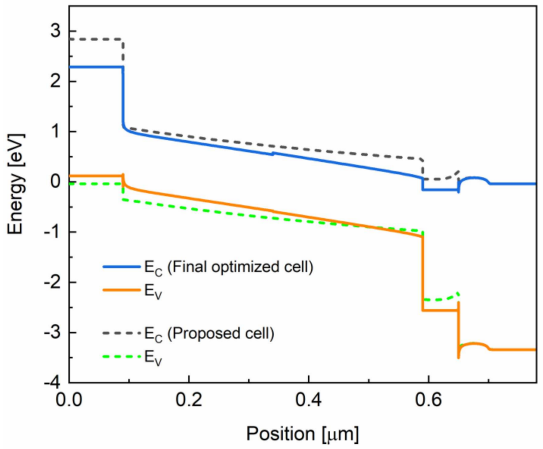

Fig. 11. Energy band diagrams of the proposed and final optimized antimony selenosulfide-based devices.

Besides, VBO at the same interface is raised from 1.365 to 1.461 eV. These variations in CBO and VBO indicate that at the interface between CdS and antimony selenosulfide, the electron injection is enhanced, whereas it decreases for holes; these findings are in accordance with those reported in [53]. The use of Cu_2O as an HTL layer also contributes to increasing the slope of the absorber energy band. All the previously discussed results cause an increase in both V_{OC} and J_{SC} and, consequently, the PCE of the final optimized solar cell.

4. Conclusions

Herein, ZnO:Al/i-ZnO/CdS/$Sb_2(S,Se)_3$/HTL/ contact heterojunction solar cell structure was studied numerically using the SCAPS-1D program. First, the carriers' doping densities in the main layers were optimized. Secondly, the effect of selenium content and profile shape was investigated. Finally, the use of Cu_2O as a probable substitute for HTL material was also addressed. The results showed that the doping densities in the main layers have a great impact on the overall solar cell performance. Doping densities of 10^{21}, 10^{15}, and 10^{21} cm^{-3} in, respectively, CdS, absorber, and HTL layers gave a PCE of 16.18%. Also, the performance of the solar cell was enhanced with the increase in Se content, reaching 17.55% with a selenium content of 0.7. For its part, the investigation of the selenium gradient in the absorber has proved that the gradient content is more beneficial than the uniform one. A gradient bandgap of $Sb_2(S,Se)_3$ using a selenium gradient content in the range of 0.8–0.9 enhanced the conversion efficiency to 18.67%. Additionally, the use of Cu_2O as a hole transport layer led to an enhancement in the solar cell performance, where PCE reached a remarkable value of 19.84% (compared to 10.05% of our proposed solar cell).

Acknowledgments

The author expresses his gratitude to Marc Burgelman from Gent University, Belgium, and acknowledges him for providing the SCAPS program.

References

[1] M.A. Green, E.D. Dunlop, G. Siefer, M. Yoshita, N. Kopidakis, K. Bothe, X. Hao, *Prog. Photovolt. Res. Appl.* **31**, 03 (2023).

[2] Solar Energy Materials adn Devices Group of Renwable Energy Laboratory, A new world record 13.6% efficiency of CZTSSe solar cells by Institute of Physics, Chinese Academy of Sciences.

[3] C. Yan, J. Huang, K. Sun et al., *Nat. Energy* **3**, 764 (2018).

[4] B. Yang, L. Wang, J. Han, Y. Zhou, H. Song, S. Chen, J. Zhong, L. Lv, D. Niu, J. Tang, *Chem. Mater.* **26**, 3135 (2014).

[5] C. Qian, J. Li, K. Sun, C. Jiangb, J. Huanga, R. Tangb, M. Greena, B. Hoex, T. Chen, X. Hao, *J. Mater. Chem. A* **10**, 2835 (2022).

[6] Y. Xinga, H. Guob, J. Liua, S. Zhanga, J. Qiub, N. Yuana, J. Dingc, *J. Alloys Compd.* **927**, 166842 (2022).

[7] F. Wu, Y. Zhao, L. Yao, H. Li, Z. Huang, L. Lin, Y. Ma, S. Chen, J. Li, G. Chen, *Chem. Eng. J.* **440**, 135872 (2022).

[8] K. Li, Y. Xie, B. Zhou, X. Li, F. Gao, X. Xiong, B. Li, G. Zeng, M. Ghali, *Opt. Mater.* **122**, 111659 (2021).

[9] X. Wang, X. Shi, F. Zhang, F. Zhou, P. Zeng, J. Song, J. Qu, *Appl. Surf. Sci.* **579**, 152193 (2022).

[10] R. Tang, X. Wang, W. Lian et al., *Nat. Energy* **5**, 587 (2020).

[11] A. Khadir, *Opt. Mater.* **127**, 112281 (2022).

[12] Y. Zhou, L. Wang, S. Chen, S. Qin, X. Liu, J. Chen, D. Xue, M. Luo, Y. Cao, Y. Cheng, H. Edward, *Nat. Photon.* **9**, 409 (2015).

[13] Z. Li, X. Liang, G. Li, H. Liu, H. Zhang, J. Guo, J. Chen, K. Shen, X. San, W. Yu, R.E.I. Schropp, Y. Mai, *Nat. Commun.* **10**, 125 (2019).

[14] R. Tang, S. Chen, Z.H. Zheng, Z.H. Su, J.T. Luo, P. Fan, X.H. Zhang, J. Tang, G.X. Liang, *Adv. Mater.* **34**, 2109078 (2022).

[15] P. Myagmarsereejid, M. Ingram, M. Batmunkh, Y.L. Zhong, *Nano-Micro Small* **17**, 2100241 (2021).

[16] Y.C. Choi, S.I. Seok, *Adv. Funct. Mater.* **25**, 2892 (2015).

[17] R. Kondrotas, C. Chen, J. Tang, *Joule* **2**, 857 (2018).

[18] X. Wang, J. Li, W. Liu, S. Yang, C. Zhu, T. Chen, *Nanoscale* **9**, 3386 (2017).

[19] X. Wang, R. Tang, C. Wu, C. Zhu, Tao Chen, *J. Energy Chem.* **27**, 713 (2017).

[20] Y.C. Choi, T.N. Mandal, W.S. Yang, Y.H. Lee, S.H. Im, J.H. Noh, S.I. Seok, *Angew. Chem.* **126**, 1353 (2014).

[21] C.L. Hassam, F. Sciortino, N.T.K. Nguyen et al., *ACS Appl. Energy Mater.* **4**, 9891 (2021).

[22] X. Wang, R. Tang, C. Jiang, W. Lian, H. Ju, G. Jiang, Z. Li, C. Zhu, T. Chen, *Adv. Energy Mater.* **10**, 2002341 (2020).

[23] Y. Zhang, J. Li, G. Jiang, W. Liu, S. Yang, C. Zhu, T. Chen, *Solar RRL* **1**, 1700017 (2017).

[24] M. Calixto-Rodriguez, H.M. García, M.T.S. Nair, P.K. Nair, *ECS J. Solid State Sci. Technol.* **2**, Q69 (2013).

[25] A.B. Jaimes, O.A. Jaramillo-Quintero, R.A. Miranda Gamboa, A. Medina-Flores, M.E. Rincon, *Solar RRL* **5**, 6 (2021).

[26] X. Wang, R. Tang, Y. Yin, H. Ju, S. Li, C. Zhu, T. Chen, *Sol. Energy Mater. Solar Cells* **189**, 5 (2019).

[27] D. Liu, R. Tang, Y. Ma, C. Jiang, W. Lian, G. Li, W. Han, C. Zhu, T. Chen, *ACS Appl. Mater. Interfaces* **13**, 18856 (2021).

[28] W. Han, D. Gao, R. Tang, Y. Ma, C. Jiang, G. Li, T. Chen, C. Zhu, *Solar RRL* **5**, 2000750 (2021).

[29] W. Wang, X. Wang, G. Chen, L. Yao, X. Huang, T. Chen, C. Zhu, S. Chen, Z. Huang, Y. Zhang, *Adv. Electron. Mater.* **5**, 1800683 (2019).

[30] C. Jiang, J. Zhou, R. Tang, W. Lian, X. Wang, X. Lei, H. Zeng, C. Zhu, W. Tang, T. Chen, *Energy Environ. Sci.* **14**, 359 (2021).

[31] O.A. Jaramillo-Quintero, M.E. Rincon, G. Vasquez-García, P.K. Nair, *Prog. Photovolt. Res. Appl.* **26**, 709 (2018).

[32] L. Zhang, K. Wu, J. Yu, Y. Yu, Y. Wei, *Vacuum* **183**, 109840 (2021).

[33] Y. Li, F. Li, G. Liang, W. Zheng, Y. Xu, Z. Zheng, P. Fan, *Surf. Coat. Technol.* **358**, 1013 (2019).

[34] C. Chen, W. Li, Y. Zhou, C. Chen, M. Luo, X. Liu, K. Zeng, B. Yang, C. Zhang, J. Han, J. Tang, *Appl. Phys. Lett.* **107**, 043905 (2016).

[35] C. Wu, L. Zhang, H. Ding, H. Ju, X. Jin, X. Wang, C. Zhu, T. Chen, *Solar Energy Mater. Solar Cells* **183**, 52 (2018).

[36] S. Lu, Y. Zhao, X. Wen, D.J. Xue, C. Chen, K. Li, R. Kondrotas, C. Wang, J. Tang, *Solar RRL* **3**, 1800280 (2019).

[37] Y. Pan, D. Zheng, J. Chen, J. Zhou, R. Wang, X. Pan, X. Hu, S. Chen, P. Yang, J. Tao, J. Chu, *J. Alloys Compd.* **906**, 164320 (2022).

[38] X. Wen, C. Chen, S. Lu et al., *Nat. Commun.* **9**, 2179 (2018).

[39] W. Wang, Z. Cao, L. Wu, F. Liu, J. Ao, Y. Zhang, *ACS Appl. Energy Mater.* **4**, 13335 (2021).

[40] H. Zhang, S. Yuan, H. Deng, M. Ishaq, X. Yang, T. Hou, U.A. Shah, H. Song, J. Tang, *Prog. Photovolt.* **28**, 823 (2020).

[41] R. Kondrotas, J. Zhang, C. Wang, J. Tang, *Solar Energy Mater. Solar Cells* **199**, 16 (2019).

[42] S. Rijal, D.B. Li, R.A. Awni, S.S. Bista, Z. Song, Y. Yan, *ACS Appl. Energy Mater.* **4**, 4313 (2021).

[43] L. Guo, B. Zhang, S. Li, A. Montgomery, L. Li, G. Xing, Q. Zhang, X. Qian, F. Yan, *Mater. Today Phys.* **10**, 100125 (2019).

[44] K. Shen, Y. Zhang, X. Wang, C. Ou, F. Guo, H. Zhu, C. Liu, Y. Gao, R.E.I. Schropp, Z. Li, X. Liu, Y. Mai, *Adv. Sci.* **7**, 2001013 (2020).

[45] G. Liang, X. Zhang, H. Ma, J. Hu, B. Fan, Z. Luo, Z. Zheng, J. Luo, P. Fan, *Solar Energy Mater. Solar Cells* **160**, 257 (2017).

[46] J. Luo, W. Xiong, G. Liang, Y. Liu, H. Yang, Z. Zheng, X. Zhang, P. Fan, S. Chen, *J. Alloy. Compd.* **826**, 154235 (2020).

[47] G.X. Liang, Z.H. Zheng, P. Fan, J.T. Luo, J.G. Hu, X.H. Zhang, H.L. Ma, B. Fan, Z.K. Luo, D.P. Zhang, *Sol. Energy Mater. Solar Cells* **174**, 263 (2018).

[48] Y.D. Luo, R. Tang, S. Chen et al., *Chem. Eng. J.* **393**, 124599 (2020).

[49] Y. Yin, C. Jiang, Y. Ma, R. Tang, X. Wang, L. Zhang, Z. Li, C. Zhu, T. Chen, *Adv. Mater.* **33**, 2006689 (2021).

[50] B. Yang, S. Qin, D.J. Xue, C. Chen, Y.S. He, D. Niu, H. Huang, J. Tang, *Prog. Photovolt. Res. Appl.* **25**, 113 (2017).

[51] H. Li, L. Lin, L. Yao, F. Wu, D. Wei, G. Liu, Z. Huang, S. Chen, J. Li, G. Chen, *Adv. Funct. Mater.* **32**, 2110335 (2022).

[52] T. Jiménez, D. Seuret-Jimenez, O. Vigil-Galán, M.A. Basurto-Pensado, M. Courel, *J. Phys. D Appl. Phys.* **51**, 435501 (2018).

[53] M.M. Nicolas-Marín, F. Ayala-Mato, O. Vigil-Galan, M. Courel, *Solar Energy* **224**, 245 (2021).

[54] I. Gharibshahian, A.A. Orouji, S. Sharbati, *Solar Energy* **227**, 606 (2021).

[55] M. Saadat, O. Amiri, *Solar Energy* **243**, 163 (2022).

[56] J. Ramanujam, U.P. Singh, *Energy Environ. Sci.* **10**, 1306 (2017).

[57] A. Morales-Acevedo, *Solar Energy* **83**, 1466 (2009).

[58] F. Azri, A. Meftah, N. Sengouga, A. Meftah, *Solar Energy* **181**, 372 (2019).

[59] Y. Zhong, Q. Zhang, Y. Wei, Q. Li, Y. Zhang, *Chinese Phys. B* **27**, 078802 (2018).

[60] Y. Firdaus, A. Seitkhan, F. Eisner et al., *Solar RRL* **2**, 1800095 (2018).

[61] S. Manzoor, J. Häusele, K.A. Bush, A.F. Palmstrom, J. Carpenter, Z.J. Yu, S.F. Bent, M.D. Mcgehee, Z.C. Holman, *Opt. Express* **26**, 27441 (2018).

[62] B. Barman, P.K. Kalita, *Solar Energy* **216**, 329 (2021).

[63] A. Khadir, *Acta Phys. Pol. A* **137**, 1128 (2020).

[64] A. Khadir, A. Kouzou, M. K. Abdelhafidi, in: *2020 17th Int. Multi-Conf. on Systems, Signals & Devices (SSD), Sfax (Tunisia)*, 2020 p. 621.

[65] A. Khadir, A. Gueddim, M.K. Abdelhafidi, L. Gacem, in: *2019 1st Int. Conf. on Sustainable Renewable Energy Systems and Applications (ICSRESA), Tebessa, Algeria*, 2019.

[66] M. Burgelman, K. Decock, S. Khelifi, A. Abass, *Thin Solid Films* **535**, 296 (2013).

[67] M. van Eerden, M. Jaysankar, A. Hadipour, T. Merckx, J.J. Schermer, T. Aernouts, J. Poortmans, U.W. Paetzold, *Adv. Opt. Mater.* **5**, 1700151 (2017).

[68] A. Khadir, *Opt. Mater.* **108**, 110443 (2020).

[69] M.T. Islam, A.K. Thakur, *Solar Energy* **202**, 304 (2020).

[70] G. Li, F. Guo, X. Zhou, L. Xue, X. Huang, Y. Xiao, *Opt. Mater.* **112**, 110791 (2021).

[71] Y. Xiao, H. Wang, H. Kuang, *Opt. Mater.* **108**, 110414 (2020).

[72] S.M. Sze, K.K. Ng., *Physics of Semiconductor Devices*, 3rd Edition, John Wiley & Sons, USA, 2007.

[73] A. Aissat, H. Arbouz, J.P. Vilcot, *Solar Energy Mater. Solar Cells* **180**, 381 (2018).